CONDENSED MATTER PHYSICS

Entropic elasticity and negative thermal expansion in a simple cubic crystal

David Wendt[1]*, Emil Bozin[1], Joerg Neuefeind[2], Katharine Page[2], Wei Ku[1†], Limin Wang[1‡], Brent Fultz[3], Alexei V. Tkachenko[4], Igor A. Zaliznyak[1§]

While most solids expand when heated, some materials show the opposite behavior: negative thermal expansion (NTE). In polymers and biomolecules, NTE originates from the entropic elasticity of an ideal, freely jointed chain. The origin of NTE in solids has been widely believed to be different. Our neutron scattering study of a simple cubic NTE material, ScF_3, overturns this consensus. We observe that the correlation in the positions of the neighboring fluorine atoms rapidly fades on warming, indicating an uncorrelated thermal motion constrained by the rigid Sc-F bonds. This leads us to a quantitative theory of NTE in terms of entropic elasticity of a floppy network crystal, which is in remarkable agreement with experimental results. We thus reveal the formidable universality of the NTE phenomenon in soft and hard matter.

INTRODUCTION

Near-zero or negative thermal expansion (NTE) is well known in metallic alloys of the invar ($Fe_{0.64}Ni_{0.36}$) family, where it is closely related to electronic magnetism (*1*). These alloys are widely used in applications requiring dimensional stability of metallic parts, e.g., in precision instruments, watches, and engines. Until recently, much less attention was paid to insulating NTE ceramics, which hold promise for numerous applications in electronics, optics, and medicine (*2*–*5*). Somewhat surprisingly, because of the specific crystal lattice geometry, NTE in these materials can have the same physical origin as a more common, positive thermal expansion (PTE): atomic thermal motion.

Interest in these systems was renewed with the observation of large isotropic NTE in zirconium tungstate, ZrW_2O_8, and then in the structurally related AM_2O_8, AM_2O_7, and $A_2M_3O_{12}$ phases (A = Zr, Hf, Sc, Y, ... and M = W, V, Mo, P, ...) and their solid solutions (*2*, *6*), which opened avenues for designing ceramic materials with tailored thermal expansion (*2*–*5*). These compounds have complex crystal structures, which can be viewed as three-dimensional (3D) networks of AX_6 octahedra and MX_4 tetrahedra (X = O) that share the corner X atoms and, most importantly, contain nearly straight, twofold-coordinated M-X-M and M-X-A linkages [the so-called open framework structures (*2*)].

NTE in such a structure can be explained by the transverse thermal motion of anion atoms, X, in the presence of the strong M-X bond, which has small or negligible thermal expansion: the so-called guitar string effect (*2*, *7*, *8*). As the amplitude of the anion transverse vibration increases with temperature, the metal atoms in M-X-M linkages are pulled closer together, thus causing the net contraction of the structure. While this simple picture does not consider the correlated motion of nearby X anions caused by their interactions in the lattice, in what follows, we show that it provides an adequate description of NTE in ScF_3 (*9*).

[1]Condensed Matter Physics and Materials Science Division, Brookhaven National Laboratory, Upton, NY 11973, USA. [2]Neutron Scattering Division, Oak Ridge National Laboratory, Oak Ridge, TN 37831, USA. [3]Department of Applied Physics and Materials Science, California Institute of Technology, Pasadena, CA 91125, USA. [4]CFN, Brookhaven National Laboratory, Upton, NY 11973, USA.
*Present address: Stanford University, Stanford, CA 94305, USA.
†Present address: Tsung-Dao Lee Institute & School of Physics and Astronomy, Shanghai Jiao Tong University, Shanghai 200240, China.
‡Present address: GE Healthcare, Chicago, IL, USA.
§Corresponding author. Email: zaliznyak@bnl.gov

An appealing model for including anion correlation considers vibrations that preserve the structure of the MX_n polyhedra, which thus move as rigid bodies, without deforming the anion-anion bonds (*2*, *10*–*13*). The relative importance of such rigid unit modes (RUMs) has been rationalized by arguing that vibrations distorting the high symmetry of the polyhedron must have a high energy cost and therefore contribute relatively little to NTE (*5*). A priori, such an ad hoc assumption is not required for the NTE effect, and its relevance has been a matter of debate (*2*, *5*, *10*–*20*). In a structure that is underconstrained, RUMs correspond to zero-energy floppy phonon modes (*5*, *10*). In a fully constrained structure, such as a cubic network of corner-sharing octahedra in ScF_3 (Fig. 1A), vibrations that do not distort polyhedra are only present on special low-dimensional manifolds occupying zero volume fraction of the system's phase space (*5*, *10*). Nevertheless, it has been argued that phonons in the vicinity of these manifolds, quasi-RUM, which involve only small distortions of the polyhedra, have special importance for NTE. ScF_3 was suggested to be a perfect example of an NTE system where the tension effect is enabled by RUM (Fig. 1B) (*5*).

RESULTS

Pair distribution function (PDF) analysis (*20*, *21*) of neutron total scattering is a powerful and direct experimental method for studying average local atomic structures and their relevance for NTE (*5*, *21*). The PDF, $g(r)$, which is obtained from the measured scattering intensity, $S(Q)$, gives the probability distribution of interatomic distances weighted by the scattering lengths of the constituent atoms and thus is uniquely sensitive to local structural patterns. Figure 1 (C to E) presents the PDF of ScF_3 measured on NPDF (C and D) and NOMAD (E) neutron diffractometers at temperatures from 2 to 1099 K. These measurements are complementary and show good agreement in the temperature range where they overlap.

An inspection of $g(r)$ curves reveals several remarkable features, of which the most important is the distinct behavior of Sc-F and F-F pair distributions. NTE of the average crystal structure is manifested by the systematic negative shift to smaller r of PDF peaks from atomic pairs with large separation, r, with increasing temperature. It is most clearly seen in Fig. 1D. The nearest F-F (≈2.8 Å) peak shows similar NTE behavior. On the other hand, the nearest-neighbor Sc-F (≈2 Å) peak shifts on heating to slightly larger r, consistent with the conventional PTE (*7*, *22*). This peak broadens only moderately with temperature, by about

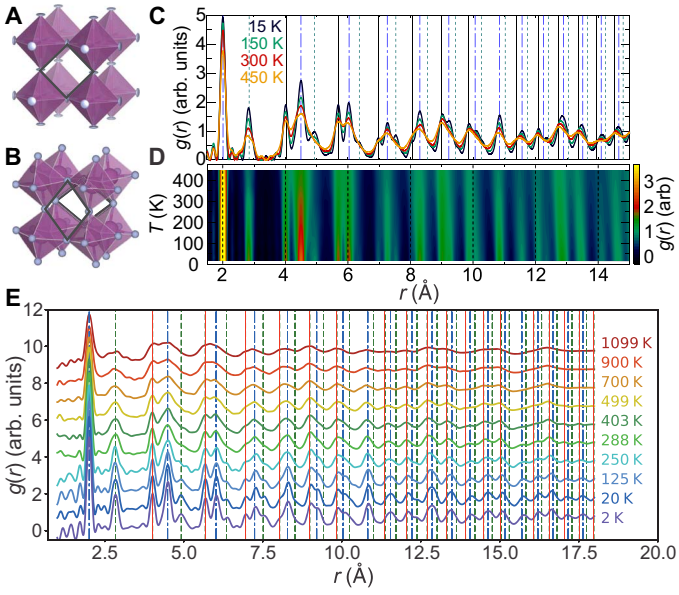

Fig. 1. Crystal structure and PDF in ScF_3. (**A**) *Pm3m* cubic perovskite crystal structure of ScF_3. Disc-shaped ellipsoids at the vertices of Sc-centered octahedra illustrate large and anisotropic thermal displacements (TDs) of fluorine atoms refined at 500 K. (**B**) Traditional ball-and-stick representation of the structure, which illustrates the octahedral tilts within the putative rigid unit motion (RUM) model. (**C**) PDF, $g(r)$, in the temperature range of 15 to 450 K obtained from neutron total scattering measurement of ScF_3 powder sample on NPDF using the wave vector range up to $Q_{max} = 27$ Å^{-1}. (**D**) The color map representation of the temperature evolution of $g(r)$ emphasizes the negative shift of peaks with increasing temperature, which is most evident at large r. (**E**) PDF measured on the same sample on NOMAD diffractometer for temperatures from 2 to 1100 K (bottom to top). Here, each curve is an average of $g(r)$ obtained using the wave vector ranges with Q_{max} varying from 23 to 32 Å^{-1} by increments of 1 Å^{-1}. For visibility, data at each temperature above 2 K are shifted upward by 1. The vertical lines in (C) and (E) mark nominal distances corresponding to Sc-F (dash-dotted), F-F (dashed), and Sc-Sc (overlapping with lattice repeats; solid) atom pairs in the ScF_3 structure.

20% at 450 K (this accounts for the decrease of peak maximum in Fig. 1), indicating a very stiff Sc-F bond. In contrast, the width of the nearest F-F peak increases markedly, revealing rapid loss of F-F correlation with increasing thermal motion. Even more marked is the behavior of further-neighbor F-F distributions. The corresponding peaks [marked by dashed lines in Fig. 1 (C and E)] are only present at $T \lesssim 300$ K and entirely disappear at higher temperatures, suggesting complete loss of positional correlation between further-neighbor F atoms. Such a liquid-like F-F PDF pattern indicates randomly phased transverse local motion of F atoms and is inconsistent with the RUM model where a large number of F-F distances are constrained by the rigid unit geometry (*5*, *18*, *19*). Also see the Supplementary Materials for additional discussion.

We quantify the observed behaviors by fitting the first several PDF peaks, which are well resolved and can be uniquely associated with distance distributions of particular atomic pairs, to Gaussian distributions (Fig. 2, A to C). The results of this analysis are summarized in Fig. 2 (D to F). While the Sc-F bond shows PTE of ≈5 parts per million (ppm) at 1000 K, both Sc-Sc, $r_{Sc-Sc} = a$ [lattice repeat distance (LRD)], and the nearest F-F, r_{F-F}, distances exhibit NTE about twice larger in magnitude (Fig. 2D). The large error bars on r_{F-F} reflect marked broadening of the F-F peak with temperature. While the full width at half maximum (FWHM) of Sc-F and Sc-Sc (LRD) peaks increases by less than 50% at 1000 K, the width of the nearest F-F distribution shows nearly an order-of-magnitude larger change, increasing to nearly 1 Å (Fig. 2E). This indicates an uncertainty of the nearest F-F distance that is comparable to the r_{F-F} distance itself, invalidating the RUM model assumption of quasi-rigid ScF_6 octahedra.

The loss of F-F pair correlation is further revealed by the temperature dependence of the intensity of the LRD (≈ 4 Å) peak (Fig. 2F). It contains partial contributions from both nearest-neighbor Sc-Sc and next-nearest-neighbor F-F pairs, in proportion $\sigma_{Sc} : 3\sigma_F \approx 1.6$, where σ_{Sc} and σ_F are coherent scattering cross sections of Sc and F, respectively. A PDF peak presents the probability distribution of interatomic distance; therefore, its integral intensity must be temperature independent. This roughly holds for Sc-F peak. A small systematic drift of its intensity, which is likely caused by T-dependent background, is within the error bar of the average value. In contrast, the LRD peak rapidly loses a substantial part of its intensity above ≈300 K, where F-F correlations disappear. The decrease is consistent with the loss of the entire ≈40% partial contribution of F-F pairs, which, above ≈300 K, contribute to broad background rather than to the narrow LRD peak described by the fit.

Motivated by these observations, we use a simple model for the probability distribution of the nearest F-F distance, which is presented in Fig. 3. It assumes uncorrelated thermal motion of individual F atoms, which is subject to a single constraint of the rigid Sc-F bond. If Sc atoms were fixed at the nodes of ScF_3 lattice, then the constraint would result in F atoms following ring trajectories with the Sc-F bond sweeping a cone. The resulting r_{F-F} probability distribution would be that of a distance between two points randomly positioned on the two nearest rings. This model has no adjustable parameters because the radius of the rings, $r_\perp$ (the average transverse deviation of F), and $r_{Sc-Sc} = a$ are obtained from the Rietveld refinement of the coherent Bragg scattering contained in our data (Fig. 4, B and C).

The model can also be set up using Sc-F and Sc-Sc distances obtained from PDF peaks in Fig. 2, although the accuracy of this refinement is lower. While larger systematic error in this approach affects some of the analysis below ≈200 K where changes are weak, above this temperature, this analysis gives results in close agreement with Figs. 3A and 4A.

Unexpectedly, when broadened by convolution with the Gaussian of the same width as Sc-F peak at 2 K to account for experimental resolution (truncation), our oversimplified model provides adequate description of the measured F-F distribution for all temperatures where NTE is observed (dashed lines in Figs. 3A and 4A). In this model, the peak maximum follows lattice NTE, in agreement with Fig. 2D. The model can be further improved if, instead of rings [or conventional Gaussian thermal displacement (TD) ellipsoids; Fig. 3B], F atoms are randomly positioned on a torus-shaped Gaussian distribution peaked at the same major diameter, $2r_\perp$, and with the minor diameter representing the F part of the Sc-F peak FWHM (Fig. 3C). This improved model conjectured by Sleight (*2*) provides slightly better agreement with the data (Fig. 3A), as quantified by the reduced mean square deviation, χ^2, presented in Fig. 4A. The χ^2 analysis is a standard way to evaluate the goodness of fit: Where $\chi^2 \approx 1$, the data are indistinguishable from the model. With $N \approx 11$ effectively independent data points used in our comparison, $\chi^2 < 3$ places the model within 3σ interval or above 99.5% likelihood level. The model begins to fail above ≈700 K, where χ^2 increases to ~10, but NTE also fades. Below ≈200 K, the broadening of the F-F peak is small and $\chi^2 \lesssim 1$,

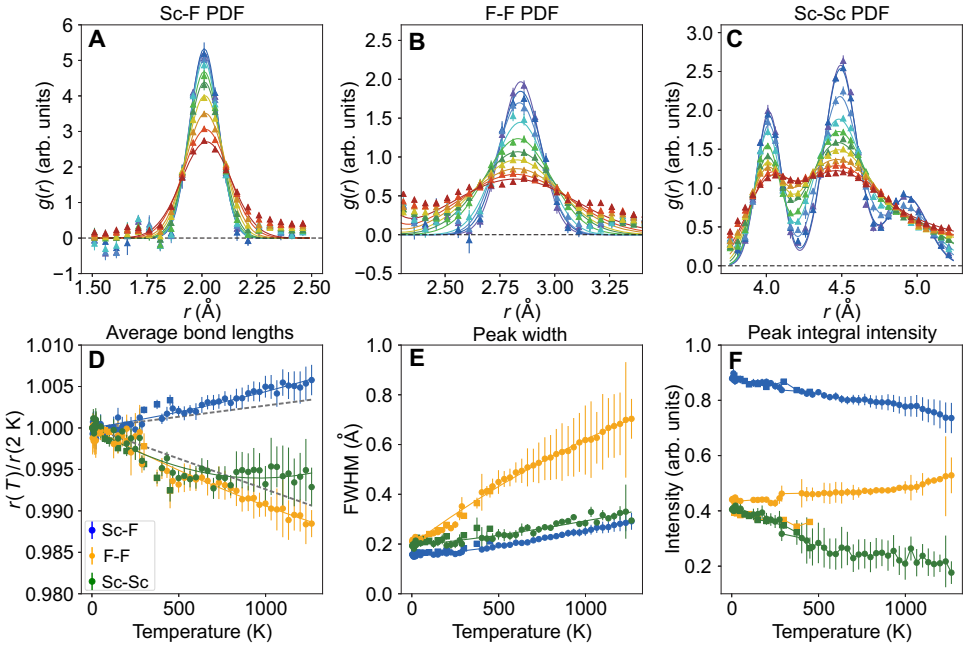

Fig. 2. Pair probability distribution for the nearest-neighbor Sc-F, F-F, and Sc-Sc (LRD) pairs. PDF data for Sc-F (**A**), F-F (**B**), and Sc-Sc [(**C**), left peak] for the same selected temperatures and with the same color coding as in Fig. 1E (symbols) with Gaussian fits (solid lines). The first two peaks, which correspond to nearest-neighbor Sc-F and F-F pairs, can be isolated and were fitted individually taking into account a small intensity overlap, which was either subtracted from the data (A) or added to the fit (B): A small overlapping intensity contribution of the F-F (≈2.8Å) peak to the Sc-F (≈2.Å) peak is seen in (B); this contribution has been computed from the model (see text) and subtracted from the data in (A). Because of an overlap of the LRD (≈4 Å) peak with the next-nearest Sc-F and next-next-nearest F-F peaks, all three were fitted together to a sum of Gaussians, within the data range [3.75 Å, 5.25 Å]. (**D**) The temperature dependence of the bond lengths obtained from the Gaussian peak position in (A) to (C) shows normal thermal expansion of the Sc-F bond and the contraction of the lattice repeat and the F-F bond. (**E**) FWHM of the PDF peaks, reflective of the atomic thermal motion. The broadening of the F-F peak is anomalous. Solid lines in (D) and (E) show fits to quadratic polynomial serving as guides for the eye; dashed lines in (D) are our prediction from entropic elasticity theory for Sc-F and Sc-Sc distances. (**F**) The integral intensities of the PDF peaks count the participating atoms and nominally should be *T* independent; the anomalous loss of the lattice repeat (Sc-Sc) peak intensity indicates loss of the coherent fluorine contribution. Circles are obtained from the NOMAD data, and squares are obtained from the NPDF data. The error bars show 1 SD accounting for the systematic error; the truncation error in (A) to (C) was estimated by averaging PDFs obtained from the data truncated at different Q_{max} values, from 23 to 32 Å^{-1}.

which means that within the experimental error, our model cannot be distinguished from other models, such as RUM.

DISCUSSION

The essential implication of our analysis is that thermal motion of even the nearest F atoms is uncorrelated rather than in RUM (Fig. 3, D and E). The spread of the F-F PDF peak with temperature follows from the increase in size of the manifold (circle or torus) populated by each F atom in the course of its thermal motion. Underlying this model is the phenomenon of energy scale separation, where two very different energies govern longitudinal and transverse motion of the F ion.

Then, in some temperature range, transverse modes can be thermally excited and the corresponding degrees of freedom can be equipartitioned, while longitudinal vibrations are still frozen out. In this case, Sc-F bonds are rigid, while F transverse vibrations are uncorrelated. Inspection of the vibrational spectra measured in ScF_3 (*17*, *18*, *22*) reveals two major phonon groups, which give rise to maxima in the density of states below $\hbar\omega_t \approx 22$ meV and above $\hbar\omega_l \approx 62$ meV. These correspond to transverse and longitudinal vibrations, respectively. This separation of energy scales implies that transverse degrees of freedom are thermally excited and equipartitioned at $T > \hbar\omega_t/k_B \approx 260$ K (k_B is Boltzmann constant), while the longitudinal rigidity of the Sc-F bond persists up to at least $T \approx \hbar\omega_l/k_B \approx 710$ K. This is exactly the temperature range where NTE is observed and where our model provides very good description of the PDF data (Fig. 4).

The exceptional longitudinal rigidity of the Sc-F bond, which underlies the NTE mechanism in ScF_3, is rooted in covalence, where the hybridization of Sc and F electronic orbitals that lie deep inside the valence band is responsible for the large energy cost of changing the Sc-F distance (*23*–*26*). Also see the Supplementary Materials for additional discussion. This Lewis-type dative bonding, where paired electrons delocalize between ions to lower their kinetic energy, has recently been described as a "charge transfer bond" (*24*). Although it has long been known that ScF_3 is anomalous among supposedly ionic metal trifluorides, MF_3 (M = Al, Sc, Fe, In, ...) (*27*), only relatively recently has the exceptional strength of the Sc-F bond been traced to the covalent nature of the valence molecular orbitals (MOs). The comparative analysis of the x-ray photoemission spectra and the density functional theory (DFT) electronic structure calculations (*25*) for the $(ScF_6)^{3-}$ cluster have indicated a large contribution to the Sc-F bonding energy of a specific ($5a_1$) $d - p$ MO at ≈ − 5 eV. A modest hybridization ($|5a_1\rangle \approx 0.83 \mid F2p\rangle + 0.16 \mid Sc3d\rangle$) does not lead to sizeable charge transfer such that Sc^{3+} and F^- appear to be close to their nominal ionic oxidation states. We performed DFT electronic structure calculations in ScF_3, which further support these findings, indicating slightly hybrid valence bands below ∼ − 4 eV and strong anisotropy of the effective potential of F ions (*26*). Also see the Supplementary Materials for additional discussion.

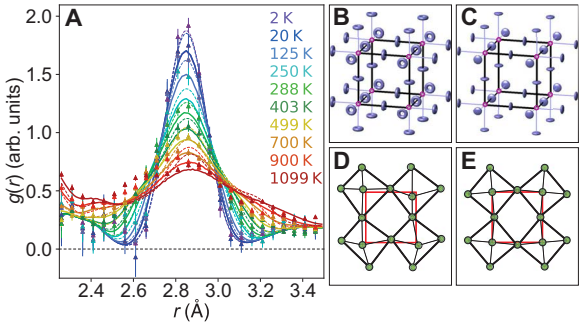

Fig. 3. Model for the fluorine motion and pair distance distribution. (**A**) PDF for the nearest-neighbor F-F bond (symbols, same as in Fig. 2B). The dashed lines show a simplified model for the F-F probability distribution, where positions of the fluorine atoms are randomly distributed on the circles whose radius is determined by the measured TD parameter obtained from Rietveld refinement. The model was broadened by convolution with the Gaussian of the same width as Sc-F peak at 2 K to account for Sc zero-point motion and truncation effects. The solid lines show an improved model, where circles are replaced by the torus-shaped Gaussian distributions peaked at the same major radius and with the width, represented by the minor radius, which is equal to $1/\sqrt{2}$ of the Sc-F peak width. The model adequately captures the evolution of the F-F peak position with temperature (Fig. 2D). (**B**) ScF_3 structure illustrating our model with the tori populated by F thermal motion under the constraint of a rigid Sc-F bond. (**C**) Traditional representation of the same structure using atomic TD ellipsoids. Both are shown for parameters refined at 500 K. (**D**) In our model, the entropic motion of F atoms distorts the fluorine octahedra, thereby erasing F-F positional correlation, in agreement with the experiment. (**E**) Opposite to what is observed, rigid octahedra in the RUM model preserve the nearest-neighbor F-F bond and also partially preserve the next-nearest-neighbor F-F correlation, which contributes to the LRD peak.

These observations immediately suggest a simple theoretical description of the NTE effect, where each Sc-F bond is treated as a rigid monomer link and the entire ScF_3 crystal structure is treated as a floppy network of such freely jointed monomers, a direct 3D analog of the celebrated model of polymer chains (Fig. 3, B and D) (*28*, *29*). Without electrostatic interactions, the network is underconstrained (floppy): The number of constraints imposed by rigid Sc-F links is six per unit cell, while the number of degrees of freedom is 12. In particular, the motion of the Sc ion is constrained by rigid bonds in all three directions, while each of the F ions has two zero-energy displacement modes corresponding to motion orthogonal to the Sc-F bond. In the absence of external tension, the system has no rigidity and would collapse. In ScF_3, net Coulomb repulsion between charged ions provides tension (negative pressure), which stabilizes the system and balances its entropic elasticity (see the Supplementary Materials for additional discussion).

We thus separate interactions in the system into a sum of the nearest-neighbor pair potentials, which include the cumulative effect of electrostatic Coulomb attraction, core repulsion, and covalent bonding and, in the simplest approximation, are treated as rigid links and the remaining Coulomb potential of non–nearest-neighbor ions. The resulting effective Hamiltonian for the fluorine transverse motion is (see the Supplementary Materials for additional discussion)

$$H = K + \frac{3N(6-M)e^2}{4\pi\epsilon_0 r} - \sum_i \frac{\tilde{\gamma}e^2}{4\pi\epsilon_0 r^3}\frac{\mathbf{u}_{i\perp}^2}{2} \qquad (1)$$

where K is the kinetic energy, $M \approx 2.98$ is the Madelung constant for ScF_3 lattice, $r = a/2$ is half of the lattice repeat, N is the number of sites, e is the electron charge, ϵ_0 is the vacuum permittivity, $\mathbf{u}_{i\perp}$ is the transverse displacement of the F ion at lattice site i, and $\tilde{\gamma} \approx 1.8$ was obtained by lattice summation of Coulomb interactions, similarly to the Madelung constant (See the Supplementary Materials for additional discussion). On account of the rigid link constraint, Hamiltonian (Eq. 1) describes the F floppy modes as independent Einstein-type oscillators with the frequency, $\hbar\omega_0 = \hbar e\sqrt{\frac{(6-M-\tilde{\gamma})}{4\pi\epsilon_0 r^3 m_F}} \approx 21.6$ meV. This value compares very favorably with the phonon dispersions measured in ScF_3, where low-energy peaks in the density of states are observed below $\hbar\omega_t \approx 22$ meV.

Although the Einstein approximation is expected to perform poorly at low temperatures, where the exact phonon dispersions are important for determining the bulk thermodynamic properties such as heat capacity or thermal expansion, it works well at $k_B T > \frac{1}{2}\hbar\omega_0$, where the equipartition theorem sets the thermal average of an oscillator Hamiltonian to $k_B T$ per degree of freedom. In this regime, heat capacity obeys the Dulong-Petit law, which is equally well described by both Einstein and Debye models. We thus expect our description, Eq. 1, to be applicable for $T \gtrsim 130$ K. Because each of the F floppy modes has a Hamiltonian of an oscillator with frequency ω_0, the value of $\langle u_\perp^2\rangle = \langle u_{i\perp}^2\rangle$ can be found with the full account for quantum effects and for an arbitrary temperature (*23*). We thus obtain the NTE effect, $\frac{r-r_0}{r_0} \approx -\frac{\langle u_\perp^2\rangle}{2r_0^2} \approx \alpha T$, where r_0 is r at $T = 0$ and $\alpha = -\frac{(4\pi\epsilon_0 r_0 k_B)}{(6-M-\tilde{\gamma})e^2} \approx -10.1\cdot10^{-6}\mathrm{K}^{-1}$, in an impressive agreement with the experimental value (Fig. 4C) (*9*).

An account for the finite rigidity of the Sc-F bond is done by replacing the rigid link constraint with an interaction potential, $V_b(r_b) \approx V_b(r_0) + f_0(r_b - r_0) + \frac{1}{2}k(r_b - r_0)^2$. Here, r_b is the bond length, f_0 is the tension force that Sc-F linkage provides to compensate the negative electrostatic pressure, and k is the effective harmonic spring constant (see the Supplementary Materials for additional discussion). From the measured frequency of the longitudinal Sc-F phonon mode, $\hbar\omega_l \approx 62$ meV, we estimate that $kr_0^2 \approx 26$ eV, which is in good agreement with our DFT results (see the Supplementary Materials for additional discussion). The minimization of the resulting free energy, which includes the entropic term, electrostatics, and bond potential, $V(r_b)$

$$F = 3N\left[-k_B T \ln\left(r_b^2 - r^2\right) + \frac{(6-M)e^2}{4\pi\epsilon_0 r} - \frac{\tilde{\gamma}e^2}{4\pi\epsilon_0 r^3}\frac{(r_b^2 - r^2)}{2} + 2V_b(r)\right] \qquad (2)$$

with respect to both r and r_b, yields the equilibrium values $r = r(T)$ and $r_b = r_b(T)$. We thus obtain the relation $\frac{r-r_0}{r_0} - \frac{r_b-r_0}{r_0} \approx \alpha T$, which means that the net entropic tension effect is split between PTE of the Sc-F bond and NTE of the lattice. It further yields the relation $\frac{r_b-r_0}{r_0} = -\beta\frac{r-r_0}{r_0}$, where $\beta \approx 0.36$, which determines the relative split between the two effects, $\frac{r_b-r_0}{r_0} = \frac{\alpha\beta}{1+\beta}T \approx 2.7\cdot10^{-6}T$ and $\frac{r-r_0}{r_0} = \frac{\alpha}{1+\beta}T \approx -7.4\cdot10^{-6}T$ (see the Supplementary Materials for additional discussion). These predictions are shown by dashed lines in Figs. 2D and 4C, which demonstrate remarkable agreement of our simple theory with experiment. We note that in our estimates, we neglected the covalent reduction of the ionic charge on F and Sc ions, which would increase the predicted NTE effect by ≈20%. This provides a ballpark estimate for the accuracy of our predictions. The leading effect of the presence of defects, such as F vacancies, or dipolar defects, which consists of a proportional change of the negative electrostatic pressure and, correspondingly,

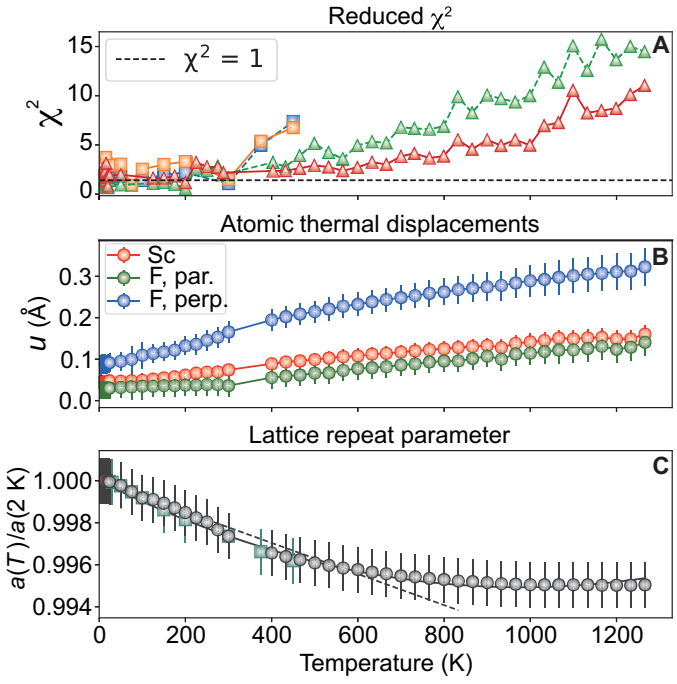

Fig. 4. The rigid-bond entropic elasticity model and NTE in ScF_3. (**A**) Reduced χ^2 quantifying the accuracy of the entropic model presented in Fig. 3 in describing our NOMAD (triangles) and NPDF (squares) data. Symbols connected by the dashed line show χ^2 for the simplified model with circles in place of tori, which is consistently slightly higher. (**B**) Atomic TD parameters and (**C**) lattice repeat, $a(T)/a$ (2 K), obtained from the Rietveld refinement of our neutron powder diffraction data, which are used to model the F-F probability distribution. Note that our model has no adjustable parameters: All numbers needed for the simulated F-F probability distribution (the lattice repeat and the F and Sc TD) are obtained from an independent analysis. Where $\chi^2 \sim 1$, the model is indistinguishable from the data. Above ≈600 K, the model begins to fail, with χ^2 reaching ~10 above 800 K. This is consistent with the failure of its basic assumption of the longitudinally rigid Sc-F bond, which is not unexpected at these high temperatures where the population of the Sc-F longitudinal (≈62 meV) phonon vibrations becomes significant (*17*). At the same time, the NTE effect fades away (C), indicating that its entropic origin is adequately captured by our model. Note that, at these high temperatures, the fluorine transverse TD approaches 10% of the nearest-neighbor distance [(B) and Fig. 2E], which is close to the Lindemann melting criterion (*1*).

the bond tension, can also be included in the effective charge. The corresponding correction to the NTE behavior is well within our estimated accuracy.

We conclude that floppy vibration modes associated with the transverse fluorine displacement in an underconstrained network crystal structure of ScF_3 give rise to both NTE of the lattice and positive expansion of the Sc-F bond. The latter effect is distinct from the conventional PTE based on cubic anharmonism of Sc-F bond potential, $V_b(r_b)$ (*30*). Instead, it originates from entropic elasticity via floppy modes and is already present for the harmonic Sc-F bond. RUM-like correlated vibration modes, which are important for understanding the stability of the cubic crystal structure, appear not to be essential for NTE.

CONCLUSION

In ZrW_2O_8, the RUM model was challenged by x-ray absorption fine structure studies (*14*) but later was argued to be consistent with neutron PDF measurements (*5*, *12*, *13*). However, for a complex material with more than three different atom types, PDF analysis has a degree of uncertainty because the measured PDF is a sum of PDFs from all atomic pairs where some features may overlap, meaning that it is difficult to identify individual peaks with specific atomic pairs (*5*). This problem is absent in ScF_3, which has a simple cubic structure with only two atom types. In agreement with the earlier molecular dynamics simulations (*17*), our present results do not support the presence of RUM, indicating that the only rigid unit is the Sc-F bond. This makes the ScF_3 structure an underconstrained 3D analog of a freely jointed polymer chain.

Our results are directly applicable to other materials with the ScF_3 structure, such as ReO_3, where NTE is observed at ≲200 K (*31*), or AlF_3, where NTE is not observed because it only adopts the cubic structure above 739 K, where conventional, positive expansion dominates (*32*).

The general design rule for inorganic NTE materials is thus the presence of a floppy network formed by nearly straight C-A-C linkages, where an underconstrained light anion, A, such as oxygen or fluorine, in a sterically open position, is strongly bound to nearby cations, C (*2*). This floppy network architecture does not imply any specific geometry of the crystal structure, such as corner-sharing octahedra network in ScF_3. This is exemplified by ZrW_2O_8 and related materials, where, when looking at a crystal structure unobscured by the coordination polyhedra, one can easily identify a network of nearly straight W-O-Zr and W-O-W linkages with an underconstrained and sterically open oxygen position. While the geometry of the resulting network and ionic positions is complex (although not as complex as in polymers), NTE in this structure can still be described using our approach, albeit requiring more cumbersome calculations of electrostatics.

On the basis of our experimental observations, we developed a simple theoretical description of the NTE effect in ScF_3, which is rooted in entropic elasticity of an underconstrained floppy network, similar in spirit to the celebrated Flory–de Gennes theory of polymer elasticity (*28*, *29*). Our approach presents a paradigm shift, where instead of focusing on peculiar energetics of low-energy lattice vibrations, such as RUM (*2*–*5*, *7*, *9*–*11*, *30*, *33*–*35*), these vibrations are approximated by Einstein local phonon modes, and the focus is on their entropic contribution to free energy. Our results provide not only a clear understanding of the entropic elasticity origin of the NTE effect in the practically important class of materials and temperature range, including at and above room temperature, but also an accurate, quantitative, textbook description of NTE, thus opening new avenues for predictive modeling of this effect in solids.

MATERIALS AND METHODS

Neutron scattering measurements for temperatures from 2 to 1266 K were carried out with NOMAD, a time-of-flight total scattering diffractometer at the Spallation Neutron Source, Oak Ridge National Laboratory, using the polychromatic neutron beam. Additional measurements for temperatures from 15 to 450 K were performed using a similar setup with an NPDF total scattering diffractometer at the Manuel Lujan Neutron Scattering Center, Los Alamos National Laboratory. For these measurements, finely pulverized polycrystalline sample (grain size, <50 μm) of cubic ScF_3 crystals (99.99% purity) was loaded into extruded vanadium containers with outer diameter of 1 cm and height of 4 cm. The same sample was used in (*17*).

For NOMAD measurements, the setup used an Orange cryostat for measurements between 2 and 300 K and an ILL furnace for measurements between 300 and 1266 K. For the NPDF experiment, the

sample was placed in a closed-cycle cryofurnace. The data at each temperature were collected for 15 to 30 min (NOMAD) and 120 min (NPDF) after the temperature equilibration. The Rietveld analysis of Bragg scattering in the obtained neutron powder diffraction data provided accurate information about the average atomic positions and the thermal mean square displacements of atoms in the crystal lattice (Fig. 4).

The atomic PDF analysis based on total scattering approach yields local structural information on different length scales (*21*), allowing refinement of the mutual positions of nuclei in different atomic pairs. The reduced PDF, $G(r)$, is obtained from the measured total scattering structure factor, $S(Q)$, via a Fourier sine transform, $G(r) = 4\pi r(\rho(r) - \rho_0) = \frac{2}{\pi}\int_0^\infty Q(S(Q) - 1)\sin(Qr)dQ$. Here, ρ_0 is the scattering cross-section weighted atomic number density of the material and $\rho(r)$ is the atomic PDF, which we analyze. It is related to the radial distribution function (RDF), $R(r) = 4\pi r^2\rho(r) = rG(r) + 4\pi r^2\rho_0$, which has the useful property that the quantity $R(r)dr$ gives the effective number of atoms in an annulus of thickness dr at a distance r from the given atom, and its integral counts the number of atoms. Both RDF and PDF were considered in this study. In our modeling, we analyzed the atomic PDF, $\rho(r) = R(r)/(4\pi r^2)$, which determines the probability for a pair of atoms to be at a distance r (Figs. 1 to 3).

In practice, the $S(Q)$ total scattering data are measured only within a limited range of wave vectors, Q. The upper limit of integration in the Fourier transform determining the experimental $\rho(r)$ has to be chosen at some finite value, Q_{max}, which includes the data where the measurement accuracy is acceptable. Different Q_{max} values lead to different weighting of the noisier data at large Q. The truncation of the Fourier transform also introduces systematic error in $\rho(r)$ in the form of the finite width of the PDF peaks and an oscillating "background" baseline ("truncation wiggles") (*20*, *21*), which depend on Q_{max}. To evaluate these systematic errors, we analyzed data computed using different Q_{max} values. The nominal Q range covered in our study is [0.5, 35] Å^{-1}. The data were extrapolated to $Q = 0$ and Fourier-transformed using the wave vector ranges, $[0, Q_{max}]$, for Q_{max} varied from 23 to 32 Å^{-1} by increments of 1 Å^{-1}. The $g(r)$ data shown in the figures here, with the exception of Fig. 1 (C and D), were obtained by averaging the data from each Q_{max} range. The error bars account both for the average statistical uncertainty and for the systematic truncation error. The latter is evaluated as the SD of the data obtained using different Q_{max} values. The obtained $g(r)$ data were modeled using custom-made Python scripts.

The model for F-F pair probability distribution was constructed as follows. Considering the Sc-F longitudinal rigidity, the average transverse deviation, $r_\perp$, of the F atoms from the Sc-Sc bond axis and the lattice repeat parameter, a, were retrieved from Rietveld refinement of the Bragg diffraction contained in the corresponding dataset. These parameters can also be obtained from the analysis of PDF peaks; using the Pythagorean theorem, $r_\perp^2 = r_{Sc\text{-}F}^2 - (a/2)^2$, where r_{Sc-F} is the average Sc-F bond length and a is the lattice repeat parameter measured as the fitted position of the Sc-F and Sc-Sc PDF peaks, respectively. This approach provides generally similar, albeit less accurate, model description because it is less accurate in determining both the lattice repeat and the transverse F displacement. We therefore opted for using the Rietveld refined parameters for our model. The data for 47 temperatures were used. The nearest-neighbor F-F distance distribution was modeled by placing evenly spaced points on perpendicular rings of radius $r_\perp$ and center separation $\frac{a\sqrt{2}}{2}$. The distances between each pair of points (not on the same ring) were calculated, and a histogram was created from the compiled set of distances. This histogram was then convoluted with a Gaussian distribution of SD equal to that of the Sc-F peak to account for truncation error and uncertainty in Sc atomic position. A second model was then created with rings replaced by Gaussian distributions peaked at these rings, which can be represented by tori of equal major diameter and separation as the rings and with the minor diameter, equal to the Gaussian FWHM, being equal to FWHM$/\sqrt{2}$ of the Sc-F peak, thus accounting for F atomic position uncertainty instead of convolution. The remaining procedure is identical to that of the first model.

SUPPLEMENTARY MATERIALS

Supplementary material for this article is available at http://advances.sciencemag.org/cgi/content/full/5/11/eaay2748/DC1

Supplementary Text

Table S1. Scandium ionization energies, E_i(Sc) (*45*), and fluorine electron affinity, E_a(F) (*49*), used in eq. S28.

Table S2. Frozen phonon calculation of the energy change as a function of the longitudinal ($\Delta E_\parallel$) and transverse ($\Delta E_\perp$) fluorine displacement in ScF_3.

Table S3. Parameters of an effective potential, $U(x) = \frac{1}{2}kx^2 + \frac{1}{4}k_4x^4$, for the longitudinal, $U_\parallel\left(\frac{r-r_0}{r_0}\right)$, and transverse, $U_\perp\left(\frac{u_\perp}{r_0}\right)$, r_0 = 2.0Å fluorine displacement in ScF_3.

Table S4. The structural parameters of ScF_3 obtained from Rietveld refinements of NOMAD data showing the standard uncertainty for the lattice spacing, a (measured in Å), and the atomic mean square displacement parameters (measured in 0.01*Å^2), isotropic for Sc ($U_{iso\text{-}Sc}$) and anisotropic for F ($U_{par\text{-}F}$ and $U_{perp\text{-}F}$, both measured in 0.01*Å^2).

Table S5. The structural parameters of ScF_3 obtained from Rietveld refinements of NPDF data including parameters R_{wp} and R_p quantifying the goodness of the fit.

Fig. S1. Electronic band structure in ScF_3.

Fig. S2. Effective potential of the fluorine ion in ScF_3.

Fig. S3. Selected plots of Rietveld refinement of structural parameters in ScF_3.

References (*37*–*55*)

REFERENCES AND NOTES

1. C. E. Guillaume, Recherches sur les aciers au nickel. Dilatations aux temperatures elevees; resistance electrique. *C. R. Acad. Sci.* **125**, 235–238 (1897).
2. A. W. Sleight, Isotropic negative thermal expansion. *Annu. Rev. Mater. Sci.* **28**, 29–43 (1998).
3. G. D. Barrera, J. A. O. Bruno, T. H. K. Barron, N. L. Allan, Negative thermal expansion. *J. Phys. Condens. Matter* **17**, R217–R252 (2005).
4. C. Lind, Two decades of negative thermal expansion research: Where do we stand? *Materials* **5**, 1125–1154 (2012).
5. M. T. Dove, H. Fang, Negative thermal expansion and associated anomalous physical properties: Review of the lattice dynamics theoretical foundation. *Rep. Prog. Phys.* **79**, 066503 (2016).
6. T. A. Mary, J. S. O. Evans, T. Vogt, A. W. Sleight, Negative thermal expansion from 0.3 to 1050 Kelvin in ZrW_2O_8. *Science* **272**, 90–92 (1996).
7. L. Hu, J. Chen, A. Sanson, H. Wu, C. Guglieri Rodriguez, L. Olivi, Y. Ren, L. Fan, J. Deng, X. Xing, New insights into the negative thermal expansion: Direct experimental evidence for the "guitar-string" effect in cubic ScF_3. *J. Am. Chem. Soc.* **138**, 8320–8323 (2016).
8. G. Ernst, C. Broholm, G. R. Kowach, A. P. Ramirez, Phonon density of states and negative thermal expansion in ZrW_2O_8. *Nature* **396**, 147–149 (1998).
9. B. K. Greve, K. L. Martin, P. L. Lee, P. J. Chupas, K. W. Chapman, A. P. Wilkinson, Pronounced negative thermal expansion from a simple structure: Cubic ScF_3. *J. Am. Chem. Soc.* **132**, 15496–15498 (2010).
10. A. K. A. Pryde, K. D. Hammonds, M. T. Dove, V. Heine, J. D. Gale, M. C. Warren, Origin of the negative thermal expansion in ZrW_2O_8 and ZrV_2O_7. *J. Phys. Condens. Matter* **8**, 10973–10982 (1996).
11. J. Z. Tao, A. W. Sleight, The role of rigid unit modes in negative thermal expansion. *J. Solid State Chem.* **173**, 442–448 (2003).
12. M. G. Tucker, A. L. Goodwin, M. T. Dove, D. A. Keen, S. A. Wells, J. S. O. Evans, Negative thermal expansion in ZrW_2O_8: Mechanisms, rigid unit modes, and neutron total scattering. *Phys. Rev. Lett.* **95**, 255501 (2005).
13. M. G. Tucker, D. A. Keen, J. S. O. Evans, M. T. Dove, Local structure in ZrW_2O_8 from neutron total scattering. *J. Phys. Condens. Matter* **19**, 335215 (2007).
14. D. Cao, F. Bridges, G. R. Kowach, A. P. Ramirez, Frustrated soft modes and negative thermal expansion in ZrW_2O_8. *Phys. Rev. Lett.* **89**, 215902 (2002).
15. J. N. Hancock, C. Turpen, Z. Schlesinger, G. R. Kowach, A. P. Ramirez, Unusual low-energy phonon dynamics in the negative thermal expansion compound ZrW_2O_8. *Phys. Rev. Lett.* **93**, 225501 (2004).

16. Z. Schlesinger, J. A. Rosen, J. N. Hancock, A. P. Ramirez, Soft manifold dynamics behind negative thermal expansion. *Phys. Rev. Lett.* **101**, 015501 (2008).
17. C. W. Li, X. Tang, J. A. Muñoz, J. B. Keith, S. J. Tracy, D. L. Abernathy, B. Fultz, Structural relationship between negative thermal expansion and quartic anharmonicity of cubic ScF_3. *Phys. Rev. Lett.* **107**, 195504 (2011).
18. S. U. Handunkanda, E. B. Curry, V. Voronov, A. H. Said, G. G. Guzmán-Verri, R. T. Brierley, P. B. Littlewood, J. N. Hancock, Large isotropic negative thermal expansion above a structural quantum phase transition. *Phys. Rev. B* **92**, 134101 (2015).
19. S. U. Handunkanda, C. A. Occhialini, A. H. Said, J. N. Hancock, Two-dimensional nanoscale correlations in the strong negative thermal expansion material ScF_3. *Phys. Rev. B* **94**, 214102 (2016).
20. C. A. Young, A. L. Goodwin, Applications of pair distribution function methods to contemporary problems in materials chemistry. *J. Mater. Chem.* **21**, 6464–6476 (2011).
21. T. Egami, S. Billinge, *Underneath the Bragg Peaks: Structural Analysis of Complex Materials* (Pergamon Press, Elsevier, ed. 2, 2012), vol. 37.
22. S. Piskunov, P. A. Žguns, D. Bocharov, A. Kuzmin, J. Purans, A. Kalinko, R. A. Evarestov, S. E. Ali, F. Rocca, Interpretation of unexpected behavior of infrared absorption spectra of ScF_3 beyond the quasiharmonic approximation. *Phys. Rev. B* **93**, 214101 (2016).
23. L. Pauling, *The Nature of the Chemical Bond* (Cornell Univ. Press, ed. 3, 1960).
24. S. Shaik, D. Danovich, B. Braida, W. Wu, P. C. Hiberty, *New Landscape of Electron-Pair Bonding: Covalent, Ionic, and Charge-Shift Bonds* (Springer International Publishing, 2016), pp. 169–211.
25. Y. A. Teterin, A. Y. Teterin, Structure of x-ray photoelectron spectra of lanthanide compounds. *Russ. Chem. Rev.* **71**, 347–381 (2002).
26. D. Bocharov, P. Aguns, S. Piskunov, A. Kuzmin, J. Purans, Electronic structure of cubic ScF_3 from first-principles calculations. *Low Temp. Phys.* **42**, 556–560 (2016).
27. J. W. Kury, A. D. Paul, L. G. Hepler, R. E. Connick, The fluoride complexing of scandium(III) in aqueous solution: Free energies, heats and entropies. *J. Am. Chem. Soc.* **81**, 4185–4189 (1959).
28. P. J. Flory, *Statistical Mechanics of Chain Molecules* (Interscience Publishers, ed. 1, 1969).
29. P. de Gennes, *Scaling Concepts in Polymer Physics* (Cornell Univ. Press, 1979).
30. T. Barron, G. White, Heat capacity and thermal expansion at low temperatures, in *International Cryogenics Monograph Series* (Springer US, 1999).
31. E. E. Rodriguez, A. Llobet, T. Proffen, B. C. Melot, R. Seshadri, P. B. Littlewood, A. K. Cheetham, The role of static disorder in negative thermal expansion in ReO_3. *J. Appl. Phys.* **105**, 114901 (2009).
32. S. Chaudhuri, P. J. Chupas, M. Wilson, P. Madden, C. P. Grey, Study of the nature and mechanism of the rhombohedral-to-cubic phase transition in $\alpha - AlF_3$ with molecular dynamics simulations. *J. Phys. Chem. B* **108**, 3437–3445 (2004).
33. M. E. Simon, C. M. Varma, Dynamics of some constrained lattices. *Phys. Rev. Lett.* **86**, 1781–1784 (2001).
34. Y. He, V. Cvetkovic, C. M. Varma, Elastic properties of a class of solids with negative thermal expansion. *Phys. Rev. B* **82**, 014111 (2010).
35. C. A. Occhialini, S. U. Handunkanda, E. B. Curry, J. N. Hancock, Classical, quantum, and thermodynamics of a lattice model exhibiting structural negative thermal expansion. *Phys. Rev. B* **95**, 094106 (2017).
36. U. D. Wdowik, K. Parlinski, T. Chatterji, S. Rols, H. Schober, Lattice dynamics of rhenium trioxide from the quasiharmonic approximation. *Phys. Rev. B* **82**, 104301 (2010).
37. Y.-R. Chen, V. Perebeinos, P. B. Allen, Density-functional study of the cubic-to-rhombohedral transition in α–AlF_3. *Phys. Rev. B* **69**, 054109 (2004).
38. C. P. Romao, C. R. Morelock, M. B. Johnson, J. W. Zwanziger, A. P. Wilkinson, M. A. White, The heat capacities of thermomiotic ScF_3 and ScF_3–YF_3 solid solutions. *J. Mater. Sci.* **50**, 3409–3415 (2015).
39. K. A. Dill, S. Bromberg, *Molecular Driving Forces: Statistical Thermodynamics in Chemistry and Biology* (Garland Science, ed. 2, 2003).
40. I. J. Zucker, Madelung constants and lattice sums for invariant cubic lattice complexes and certain tetragonal structures. *J. Phys. A Math. Gen.* **8**, 1734–1745 (1975).
41. Y. Sakamoto, Madelung constants of simple crystals expressed in terms of Born's basic potentials of 15 figures. *J. Chem. Phys.* **28**, 164–165 (1958).
42. H. M. Evjen, On the stability of certain heteropolar crystals. *Phys. Rev.* **39**, 675–687 (1932).
43. R. D. Shannon, R. X. Fischer, Empirical electronic polarizabilities in oxides, hydroxides, oxyfluorides, and oxychlorides. *Phys. Rev. B* **73**, 235111 (2006).
44. J. D. Jorgensen, Z. Hu, S. Teslic, D. N. Argyriou, S. Short, J. S. O. Evans, A. W. Sleight, Pressure-induced cubic-to-orthorhombic phase transition in ZrW_2O_8. *Phys. Rev. B* **59**, 215–225 (1999).
45. D. R. Lide, *CRC Handbook of Chemistry and Physics* (Taylor & Francis, ed. 84, 2003).
46. D. M. P. Mingos, *The Chemical Bond II: 100 Years Old and Getting Stronger* (Springer International Publishing, 2016).
47. A. Haaland, T. Helgaker, K. Ruud, D. J. Shorokhov, Should gaseous BF_3 and SiF_4 be described as ionic compounds? *J. Chem. Educ.* **77**, 1076 (2000).
48. J. Dean, *Lange's Handbook of Chemistry* (McGraw-Hill, 1999), vol. 15.
49. C. Blondel, P. Cacciani, C. Delsart, R. Trainham, High-resolution determination of the electron affinity of fluorine and bromine using crossed ion and laser beams. *Phys. Rev. A* **40**, 3698–3701 (1989).
50. T. Kiang, R. N. Zare, Stepwise bond dissociation energies in sulfur hexafluoride. *J. Am. Chem. Soc.* **102**, 4024–4029 (1980).
51. N. Marzari, D. Vanderbilt, Maximally localized generalized wannier functions for composite energy bands. *Phys. Rev. B* **56**, 12847–12865 (1997).
52. I. Souza, N. Marzari, D. Vanderbilt, Maximally localized wannier functions for entangled energy bands. *Phys. Rev. B* **65**, 035109 (2001).
53. A. A. Mostofi, J. R. Yates, Y.-S. Lee, I. Souza, D. Vanderbilt, N. Marzari, wannier90: A tool for obtaining maximally-localised wannier functions. *Comput. Phys. Commun.* **178**, 685–699 (2008).
54. J. Kunes, R. Arita, P. Wissgott, A. Toschi, H. Ikeda, K. Held, Wien2wannier: From linearized augmented plane waves to maximally localized wannier functions. *Comput. Phys. Commun.* **181**, 1888–1895 (2010).
55. H. B. Hamed, A. Qteish, N. Meskini, M. Alouani, Calculated hybrid and semilocal functionals and *gw* electronic structure of the metal trifluorides MF_3 (M = Sc, y, al). *Phys. Rev. B* **92**, 165202 (2015).

Acknowledgments: We gratefully acknowledge discussions with C. Li, A. Abanov, and P. Allen. D.W. thanks the Condensed Matter Physics and Materials Science Division at Brookhaven National Laboratory, where part of this work was performed during his summer internship, for the hospitality. **Funding:** Work at Brookhaven National Laboratory (BNL) was supported by the Office of Basic Energy Sciences, Division of Materials Sciences and Engineering, U.S. Department of Energy, under contract no. DE-SC0012704. Work at BNL's Center for Functional Nanomaterials (CFN) is sponsored by the Scientific User Facilities Division, Office of Basic Energy Sciences, U.S. Department of Energy, under the same contract. This research at ORNL's Spallation Neutron Source was sponsored by the Scientific User Facilities Division, Office of Basic Energy Sciences, U.S. Department of Energy. **Author contributions:** I.A.Z. conceived and directed the study. I.A.Z., E.B., and B.F. designed the study. B.F. provided the sample for the study. E.B., K.P., and J.N. performed the experiments. E.B. carried out the Rietveld analysis. D.W. and I.A.Z. analyzed the data and prepared the figures. D.W. carried out modeling of the experimental PDF data. L.W. and W.K. performed DFT calculations. A.V.T. and I.A.Z. carried out the theoretical analysis. I.A.Z. wrote the paper, with input from all authors. **Competing interests:** The authors declare that they have no competing interests. **Data and materials availability:** All data needed to evaluate the conclusions in the paper are present in the paper and/or the Supplementary Materials. Additional data related to this paper may be requested from authors.

Submitted 4 June 2019
Accepted 16 September 2019
Published 1 November 2019
10.1126/sciadv.aay2748

Citation: D. Wendt, E. Bozin, J. Neuefeind, K. Page, W. Ku, L. Wang, B. Fultz, A. V. Tkachenko, I. A. Zaliznyak, Entropic elasticity and negative thermal expansion in a simple cubic crystal. *Sci. Adv.* **5**, eaay2748 (2019).